The FEBS Journal

FEBS PRESS science publishing by scientists

Gating in plant plasma membrane aquaporins: the involvement of leucine in the formation of a pore constriction in the closed state

Agustina Canessa Fortuna[1,2], Gerardo Zerbetto De Palma[1,2,3], Lucio Aliperti Car[4], Luciano Armentia[2], Victoria Vitali[1,2], Ari Zeida[5], Darío A. Estrin[6] and Karina Alleva[1,2]

1 Facultad de Farmacia y Bioquímica, Instituto de Química y Fisicoquímica Biológica (IQUIFIB), CONICET, Universidad de Buenos Aires, Argentina
2 Departamento de Fisicomatemática, Facultad de Farmacia y Bioquímica, Universidad de Buenos Aires, Argentina
3 Instituo de Biotecnología, Universidad Nacional de Hurlingham, Villa Tesei, Argentina
4 Laboratorio de Fisiología de Proteínas, IQUIBICEN y Facultad de Ciencias Exactas y Naturales, CONICET, Universidad de Buenos Aires, Argentina
5 Departamento de Bioquímica, Facultad de Medicina, Center for Free Radical and Biomedical Research, Universidad de la República, Montevideo, Uruguay
6 DQIAQF-INQUIMAE, Facultad de Ciencias Exactas y Naturales, CONICET, Universidad de Buenos Aires, Argentina

Keywords
aquaporin; gating; leucine plug; molecular dynamics; water transport

Correspondence
K. Alleva, Facultad de Farmacia y Bioquímica, Instituto de Química y Fisicoquímica Biológica (IQUIFIB), CONICET, Universidad de Buenos Aires, Junín, Buenos Aires 956, Argentina
Tel: +54 1152874552
E-mail: kalleva@ffyb.uba.ar

Agustina Canessa Fortuna and Gerardo Zerbetto De Palma contributed equally to this article

(Received 18 February 2019, revised 25 April 2019, accepted 8 May 2019)

doi:10.1111/febs.14922

The control of water permeability in plant PIP2 aquaporins has become a paradigmatic case study of the capping mechanism for pore closure in water channels. From structural data, it has been postulated that the gating process in PIP2 involves a conformational rearrangement in cytosolic loopD that generates an obstruction to the transport of water molecules inside the aquaporin pore. BvPIP2;2 is a PIP2 aquaporin from *Beta vulgaris* whose pH response has been thoroughly characterized. In this work, we study the participation of Leu206 in BvPIP2;2 gating triggered by cytosolic acidification and show that this residue acts as a plug that blocks water transport. Based on data obtained from *in silico* and *in vitro* studies, we demonstrate that Leu206, one of the residues lining the pore, is responsible for ~ 60% of water blockage. Cell osmotic swelling experiments and atomistic molecular dynamics simulations indicate that the replacement of Leu206 by an Ala residue maintains high water permeability under conditions where the pore is expected to be closed. The present work demonstrates that Leu206, located at the cytoplasmic entry of the channel, constitutes a crucial pH-sensitive steric gate regulating water transport in PIP aquaporins.

Introduction

Aquaporins (AQP) are the main channels involved in the transport of water (and other small solutes) across cell membranes [1,2]. Among aquaporins, PIP (plasma membrane intrinsic proteins) constitute the largest and most conserved plant AQP subfamily [3]. PIP subfamily is phylogenetically organized in two groups of paralogues, PIP1 and PIP2. This is an ancient specialization since both paralogues have been found even in primitive plants such as *Physcomitrella patens* [3]. PIP aquaporins have key functions in plants as these

Abbreviations
AQP, aquaporin; cRNA, complementary RNA; MSA, multiple sequence alignment; p_f, intrinsic osmotic water permeability coefficient; P_f, osmotic water permeability coefficient; PIP, plasma membrane intrinsic protein; PMF, potential mean force; POPC, 1-palmitoyl-2-oleoyl-glycero-3-phosphocholine.

channels are involved in the regulation of water flux through plasma membranes in all plant tissues and, therefore, in plant water homeostasis [4,5].

The structural and topological features of several members of the aquaporin family have been elucidated [6–13]. This structural information shows that all aquaporins share an identical architecture consistent with the 'hourglass model' [14]. Indeed, PIP channels present the typical fold found in all the other members of the aquaporin family, a main structural core of six transmembrane alpha helices and five connecting loops with N and C-terminal domains in the cytoplasmic side. The transmembrane helices are organized surrounding a single pore together with a seventh transmembrane region created by the insertion of loops B and E into the channel from opposite sides of the membrane. All PIP channels present the two main and conserved regions that regulates the specificity of transport: the Asn-Pro-Ala (NPA) motives and the aromatic/arginine (Ar/R) selectivity filter (Fig. 1). The main difference among PIP and other aquaporins is the length of loopD. This flexible structure is crucial for the open-closed transition found in PIP channels.

Analyzing the structural framework provided by the X-ray structures of spinach (*Spinacia oleracea*) SoPIP2;1 in closed and open conformations, Törnroth-Horsefield and coworkers proposed a 'capping' mechanism to explain PIP aquaporin gating [10,15,16]. This mechanism implies a large-scale rearrangement of loopD causing the capping of the channel that leads to the closed state. So, in the closed conformation, PIP's loopD appears to be folded underneath the channel and linked to the N-terminal domain and loopB through a network of salt bridges, water-mediated interactions and hydrogen bonds. Together with loopD movement, the displacement of a hydrophobic plug is proposed to occlude the PIP pore. The triggering events that promote the open-closed transition in PIP channels can be a drop in cytoplasmic pH, an increase in Ca^{2+} concentrations or the dephosphorylation of specific serine residues [17–22]. Permeability regulation by pH has been reported for different aquaporins such as mammalian AQP3, AQP4, AQP5, AQP7 and plant AtTIP2;1, VvTIP2;1 among others [23–28]. But in particular, cytosolic acidification is a well-studied trigger for PIP channels gating as pH regulation of water transport has been described in red beet, *Arabidopsis thaliana*, strawberry, grape, and tobacco PIP aquaporins [17,20,29–33]. A conserved histidine residue located in PIP's loopD (His197 in AtPIP2;1) has been

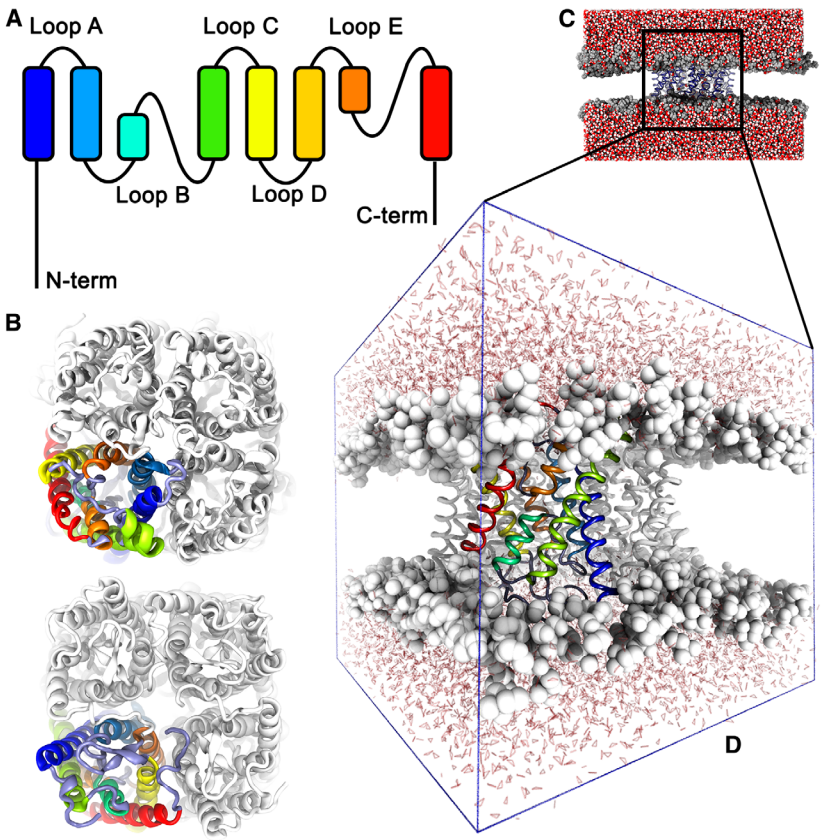

Fig. 1. General PIP aquaporin topology. (A) Intramembrane domains are shown as colored rounded squares and extracellular and cytosolic loops and termini are shown as black lines. (B) Top and bottom views of a representative PIP homotetramer as built for molecular dynamics simulations. Colors used for a monomer correspond to those shown in A. (C) General side view of the simulation box. Van der Waals representation was used for water and phosphatidylcholine groups and cartoon was used for protein. Oleyl and palmitoyl chains are not shown. (D) Detail of the embedded PIP homotetramer in the fully hydrated POPC membrane shown in C. PDB 1Z98 was used for the representations shown in B, C, and D.

shown as the main proton sensor in these channels [19,34]. However, the relevance of the hydrophobic plug in PIP gating has never been tested in aquaporins with probed proton gating.

It has been previously shown that a drop in cytoplasmic pH generates an over 95% reduction in water transport through PIP aquaporins located at the plasma membrane of red beet (*Beta vulgaris*) storage roots cells [20]. Moreover, we have characterized the pH cooperative response of BvPIP2;2 both in their homotetrameric or heterotetrameric assemblies with BvPIP1;1 [31,35]. In the present work, water permeability assays, site-directed mutagenesis, and molecular dynamics simulations are used to elucidate if the suggested hydrophobic gate participates in proton regulation of this well-characterized BvPIP2;2 channel.

Results

Leu206 forms a constriction in BvPIP2;2 water pore

As mentioned before, a hydrophobic plug was proposed to occlude the pore in PIP aquaporins. For SoPIP2;1, it was proposed that this plug is realized by a leucine residue located in loopD. BvPIP2;2 biological activity under acidification has been thoroughly characterized in previous works [30,31,35] making this aquaporin an ideal target for the elucidation of the role of loopD's leucine in proton gating. However, the only atomistic structures resolved for any PIP aquaporin correspond to SoPIP2;1 [10]. So, a detailed comparison between the general structure and pore profile of BvPIP2;2 and SoPIP2;1 is mandatory to support that the gating mechanism described for SoPIP2;1 can be generalized and applied to BvPIP2;2.

A comparative analysis of SoPIP2;1 and BvPIP2;2 sequences shows that both proteins share a 76% of amino acidic identity—they differ mainly in the extracellular loopA length—and a full conservation of all residues pointed as involved in PIP gating (Fig. 2A,B). The main residue pointed as a hydrophobic plug in SoPIP2;1 crystal structures is Leu197. This amino acid is a highly conserved residue located in PIP2's loopD (Fig. 2C) and the analogous residue to SoPIP2;1 Leu197 is the BvPIP2;2 Leu206 residue (Fig. 2A).

In order to compare SoPIP2;1 and BvPIP2;2 general structure and pore profiles, we prepared a homology model of BvPIP2;2 and performed 500-ns equilibrium simulations for each protein.

The simulations were performed for homotetrameric assemblies embedded in a fully hydrated POPC bilayer. We find that both channels share a high similarity in their general structures (Fig. 2B) but in particular, in their pore geometry (Fig. 3). The dynamic behavior shows that the pores of SoPIP2;1 and BvPIP2;2, in their closed states, present a similar profile (Fig. 3). There are two constriction zones around the Ar/R filter (conserved in all aquaporins) and the vicinity of Leu197/Leu206. As shown in Fig. 3, in BvPIP2;2 the pore radius at the Ar/R region is of approximately 0.72 Å, a similar value was previously reported for SoPIP2;1 [10] and other aquaporins [6,23,36] (Fig. 3A). Then, the channel narrows again to 1.2 Å at the vicinity of Leu206 or to 1.4 Å for SoPIP2;1 Leu197. This value of 1.4 Å was also reported for this region of SoPIP2;1 in a previous work [10]. This constriction zone extends to the area occupied by Pro195 and Val194 in SoPIP2;1 or Pro204 and Val203 in BvPIP2;2. Here, we analyzed, in particular, the proximity of Leu206 since the dispersion of radius in this part of the channel is lower than the dispersion found in the zone of Pro204 and Val203 (data not shown).

We checked the free energy profile for water transport by computing the potential mean force (PMF) in order to know the permeation barrier for water along the pore in both PIP2. Both channels present a similar profile along the pore. Higher values of PMF for water have been obtained for BvPIP2;2 in comparison with SoPIP2;1 in the zone around 12–18 Å of the channel axis. Notwithstanding, all values are among the expected ones for an energetic barrier for water in its single file transport through an aquaporin pore. It has been reported that, in single file water transport, it is not the number of water molecules in the file but the number of hydrogen bonds donors or acceptors along the pore what determines the permeability barrier to water in each individual channel [37]. So, we also analyzed the frequency of hydrogen bonding within the pore for both SoPIP2;1 and BvPIP2;2. There is a similar hydrogen bond frequency profile for both aquaporins, and, moreover, the residues' sites that can be involved in hydrogen bonding are the same and are localized in the same places in each one of the two proteins (Fig. 3).

Side chain of Leu206 is an efficient plug to block water transport in BvPIP2;2

To estimate the effect of leucine side chain in the pore constriction, we first created the *in silico* mutant, BvPIP2;2L206A. An alanine residue was chosen to replace the leucine, since alanine is an amino acid with a shorter side chain. After running 500-ns equilibrium simulations for wild-type and mutant channels in close

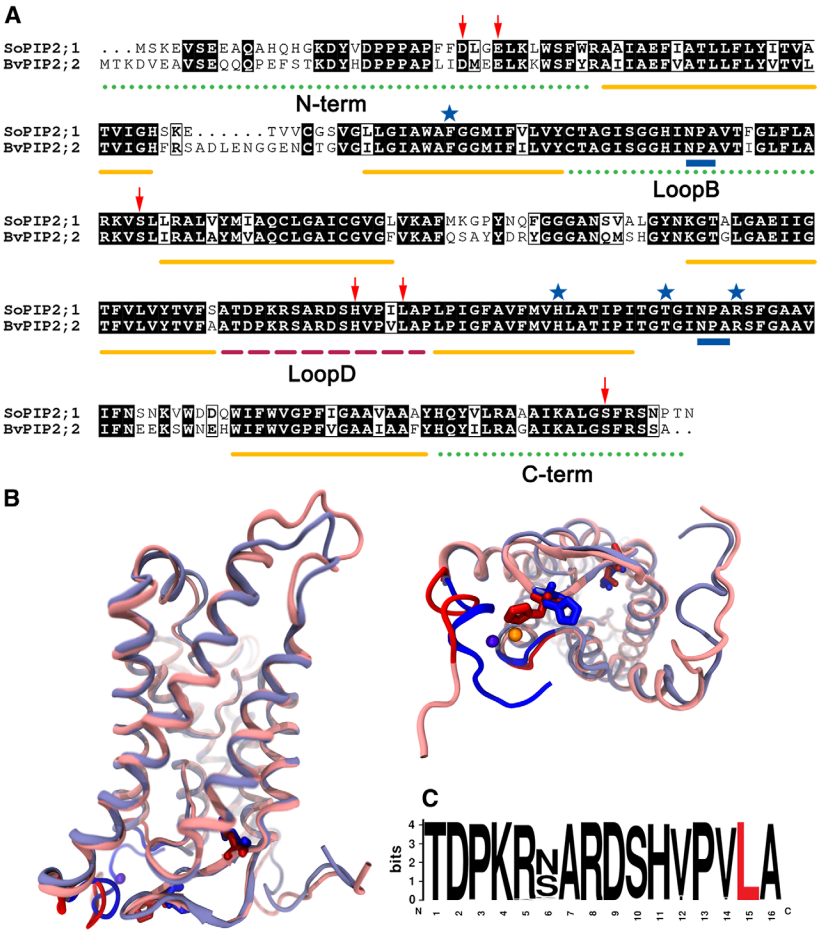

Fig. 2. Comparison of SoPIP2;1 and BvPIP2;2 sequences and structures. (A) Primary structure comparison between BvPIP2;2 and SoPIP2;1. All residues depicted to be involved in the stabilization of the closed conformation are marked (red arrows). NPA residues are underlined in blue, Ar/R filter is pointed with stars, transmembrane domains are underlined in orange, loopB, N- and C-terminal tails are underlined with dotted green lines and loopD with dashed red line. (B) Superimposition of BvPIP2;2 homology model (red) and SoPIP2;1 (blue) crystal structure, side view and cytosolic view of a monomer are shown. Residues involved in gating (loopD's His and Leu, loopB, and N terminus are marked with intense colors. (C) PIP2's loopD logo sequences, under study Leu is marked in red.

configurations and measuring intrinsic osmotic permeability (p_f) every 50-ns interval, the mutant showed a threefold increase in water permeability in comparison with the wild-type: $(5.27 \pm 0.06) \times 10^{-14}$ cm^3·s^{-1} vs. $(1.61 \pm 0.02) \times 10^{-14}$ cm^3·s^{-1}, $n = 40$, $P < 3.4 \times 10^{-12}$ (Fig. 4). This intrinsic water permeability was measured as the average of the individual p_f obtained for each monomer in the tetramers in order to consider the fluctuation that could emerge from the different time evolution that each chain has during the simulation in the studied time scale. Similar fluctuation values, intrinsic to the dynamic of the pore, has been reported before for different water transport simulations through aquaporins [38–40]. The increase in p_f calculated for BvPIP2;2L206A in comparison with wild-type BvPIP2;2 corresponds to the closed state conformations, that is, loopD capping the water pore of both channels. As it has been reported from SoPIP2;1 X-ray structure, in the closed conformation loopD caps the channel establishing contacts with the N-terminal tail while in the open conformation loopD is displaced up to 16 Å [10]. To confirm that this conformation was maintained during the simulation we assessed if the network of ionic interactions and hydrogen bonds characteristic of the PIP2 closed state was stable.

Figure 5 shows the comparison of key residues stabilizing the closed state in BvPIP2;2 and BvPIP2;2L206A structures. The superimposition of BvPIP2;2 and BvPIP2;2L206A structures shows that loopD is near N-terminal tail in both channels (Fig. 5A). We used the distance between His202 and Asp191 (located in loopD) and the geometric center of carboxyl oxygen of Asp31, Glu33, and Glu34 as an indicator of the extent of the closed state of both channels. All distances are stable during the timescale of our simulations for the wild-type and mutant channels. So, we can rule out movements of loopD as responsible of water transport increment in mutant PIP.

Finally, to assess if the change in water permeation after replacement of Leu206 by an alanine residue was due to a purely steric alteration in the pore radius or to a modified residence time of water molecules due to

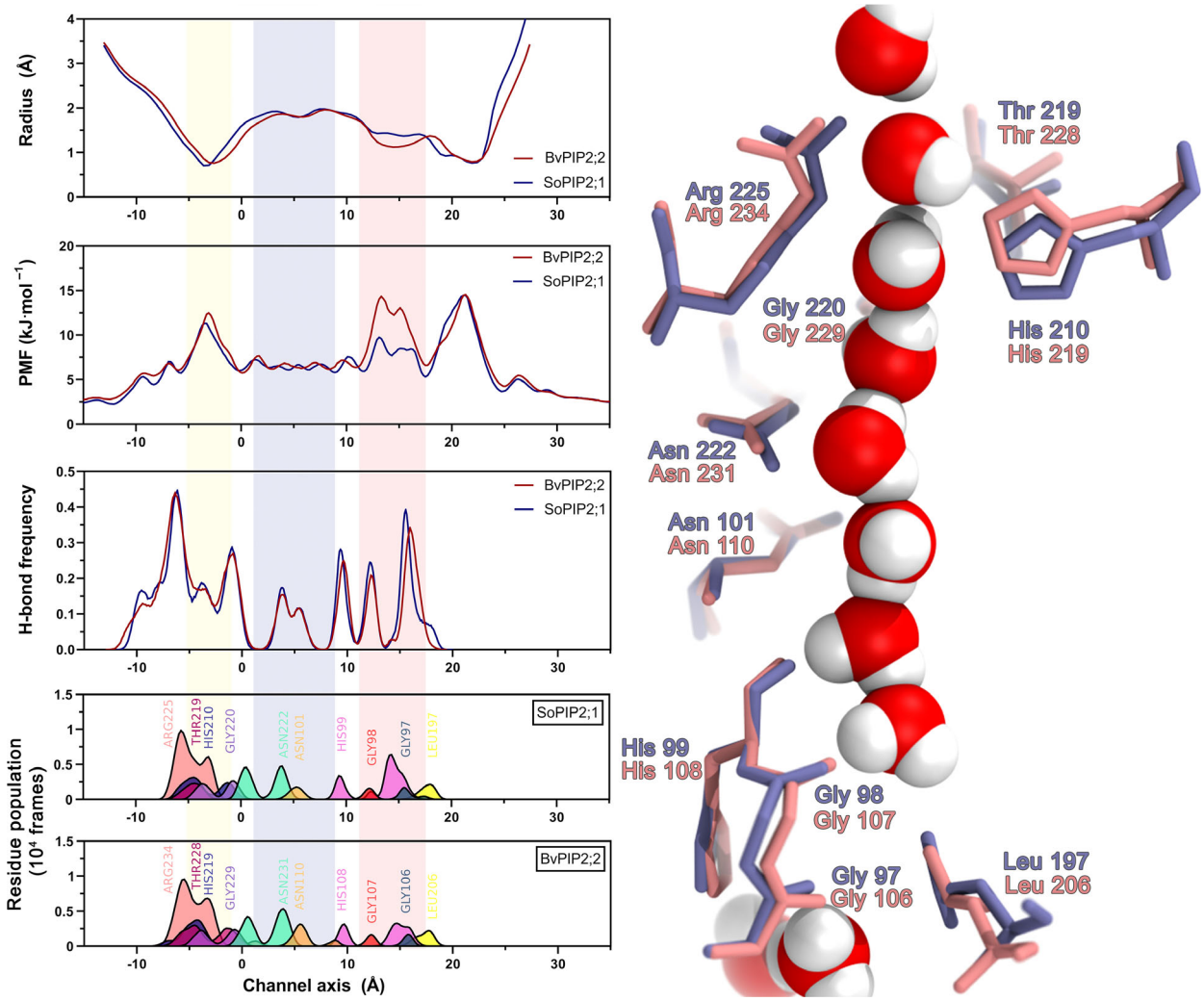

Fig. 3. Pore profile comparison between SoPIP2;1 and BvPIP2;2. Left: Mean radius (upper panel), PMF for water molecules (upper middle panel), H-bond frequency (lower middle panel) and pore lining H-bond sites population, grouped by residue (lower panels), along the channel axis. Every property was evaluated from the 500-ns-long MD simulation. The relevant zones are colored in yellow for the Ar/R filter, in blue for the NPA and in pink for the Leu zone. Right: the superimposition of SoPIP2;1 (blue) and BvPIP2;2 (pink) H-bonding pore lining residues appearing in the upper middle left panels are shown.

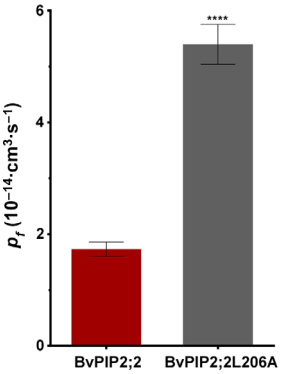

Simulation	p_f (10^{-14} cm^3·s^{-1})	Chain	p_f (10^{-14} cm^3·s^{-1})
BvPIP2;2	1.61 ± 0.02	A	2.53 ± 0.35
		B	1.48 ± 0.17
		C	1.51 ± 0.16
		D	1.40 ± 0.13
BvPIP2;2L206A	5.27 ± 0.06	A	7.30 ± 0.35
		B	3.95 ± 0.87
		C	5.54 ± 0.44
		D	4.82 ± 0.57

Fig. 4. Equilibrium intrinsic permeability for BvPIP2;2 and BvPIP2;2L206. The average permeability values (p_f) calculated in BvPIP2;2 and BvPIP2;2L206A simulations in their closed state. Data corresponding to each chain in the tetramers for each channel are shown in the left panel. The uncertainty is estimated with the SEM calculated for the trajectory, $P < 0.0001$.

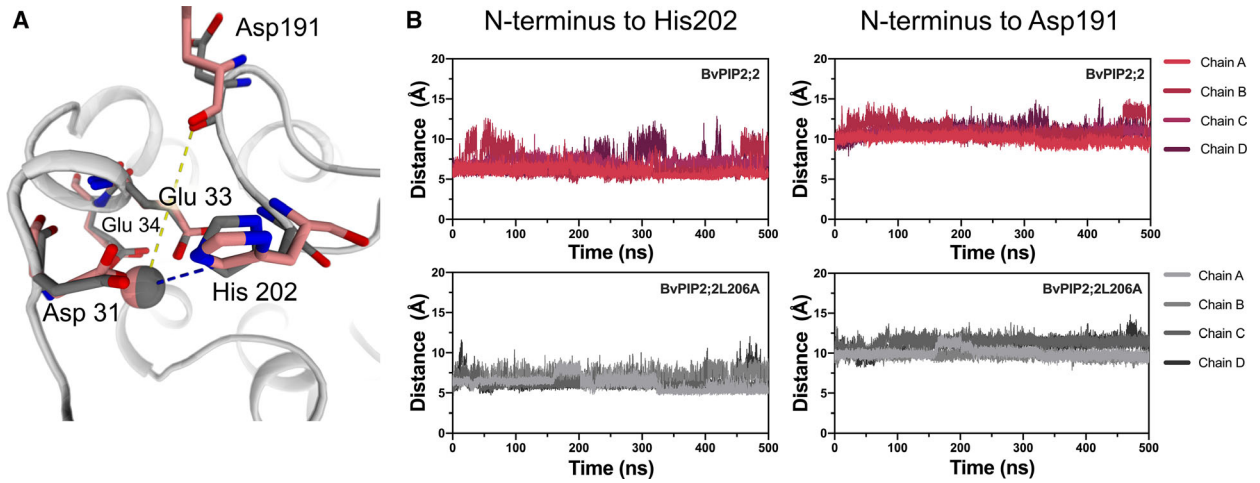

Fig. 5. LoopD interaction with N-terminal tail along the simulation. (A) Superimposition of BvPIP2;2 and BvPIP2;2L206A representative structures showing the His202-N-terminal tail (blue dashed line) and Asp191-N-terminal tail (yellow dashed line) distances taken as capping parameters. (B) His202-N-terminal tail and Asp191-N-terminal tail distances over time for each chain of the tetramers in each simulation.

any alteration in the hydrogen bonding inside the channels, we calculated the radius profile for each channel and the frequency of hydrogen bonds. Our results show that a significantly wider pore is found in the region where the Leu206 is located when this residue is replaced by an alanine (Fig. 6). The mean pore radius for BvPIP2;2L206A is 1.8 Å, a 53% higher than the mean pore radius in wild-type BvPIP2;2 at the vicinity of Leu206.

Interestingly, the constriction zone between the Z coordinates 12 and 17 Å, corresponding to the region of Leu206, presents an average minimum radius along the whole simulation of 0.6 Å for wild-type BvPIP2;2 and of 1.4 Å for the mutant BvPIP2;2L206A. This increment is enough to allow the passage of water molecules with a higher frequency. Accordingly, the PMF in that region is lowered from approximately 12.8 to 6.7 kJ·mol^{-1}. On the other hand, the hydrogen bonding profile is quite similar between wild-type and mutant channels, only subtle differences were found in the H-bond frequency in the vicinity of Leu206 with higher values for the mutant.

BvPIP2;2L206A is a functional channel and present lower sensitivity to acidification

Wild-type BvPIP2;2 and mutant BvPIP2;2L206A heterologously expressed in *Xenopus laevis* oocytes were subsequently used to evaluate the relevance of this Leu206 residue in the blockage of the pore under acidic conditions. Water permeability was evaluated by osmosis-based oocyte assays, as previously reported for this protein [30,31].

The expression of BvPIP2;2L206A leads to an increase in plasma membrane osmotic water permeability coefficient of oocytes compatible with an active water channel, $(74.6 \pm 7.4)\ 10^{-4}$ cm·s^{-1} (±SEM, $n = 10$) (Fig. 7A,B). When pH inhibition was assayed in oocytes expressing the wild-type and mutant channels, a significant difference was found (Fig. 7). While the osmotic water transport for wild-type suffers, approximately, an 80% of inhibition when internal pH 7.2 is lowered to pH 6.3, the mutant is inhibited a 33%. This result shows that the only presence of Leu206 in the closed state accounts for almost 60% of the water transport blockage that occurs under cytosolic acidification. In previous works, we reported that BvPIP2;2 presents, in similar experiments to those performed in the present work, a cooperative behavior with a value for $pH_{0.5}$ of approximately 6.4–6.5 [35]. Here, we also test the complete dose–response curve of biological activity (P_f) vs. internal proton concentration for the mutant employing the wild-type channel as control. It can be seen that while $pH_{0.5}$ (6.45 ± 0.01, ±SEM, $n = 3$) is conserved, the minimum P_f in oocytes expressing the mutant is reached at only a ~ 30% lower value from the maximum values. These data indicate that there is a lack of inhibition in the mutant without altering the cooperativity of the response (Fig. 7D). As we previously characterized the BvPIP2;2–BvPIP1;1 interaction [31], here we coexpressed BvPIP2;2L206A with BvPIP1;1. This experiment allows us to control if the mutation does not alter the interaction among PIP paralogue monomers within the tetramer. The coexpression of equal amount of complementary RNA (cRNA) coding for BvPIP2;2L206A and BvPIP1;1 promotes an approximately

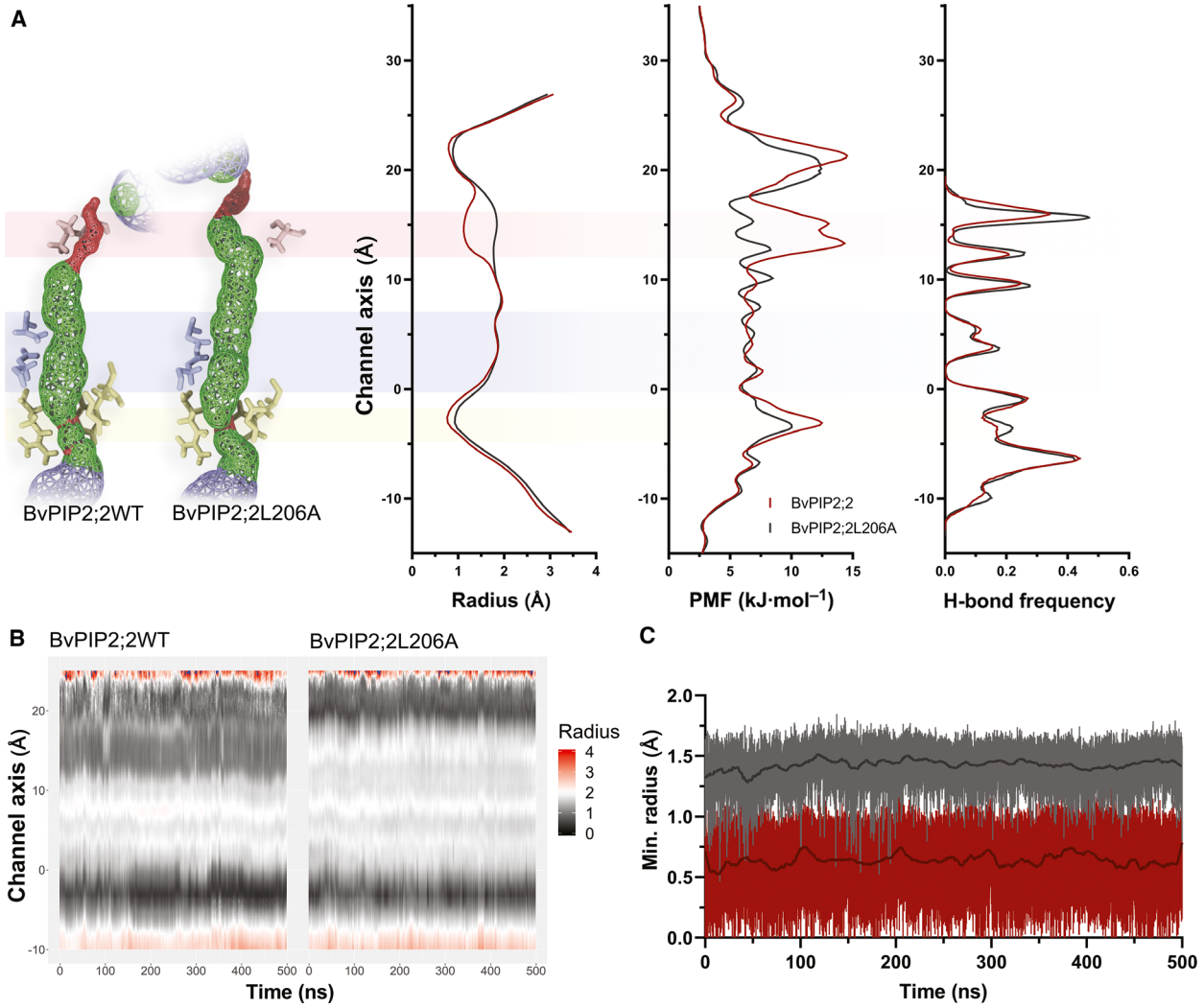

Fig. 6. Pore profile comparison between wild-type BvPIP2;2 and BvPIP2;2L206A. (A) From left to right: Pore lumen representation, pore radius, PMF, and H-bond frequency along the pore axis. The zones corresponding to constrictions are colored, yellow for the Ar/R filter, blue for the NPA and pink for the Leu zone. (B) Pore radius (in Å) for each Z coordinate along the whole simulation, represented in color scale for chain D of wild-type BvPIP2;2 (left panel) and BvPIP2;2L206A (right panel). Main differences are around Z = 15.5 Å, which corresponds to the Leu region. (C) Minimum pore radius in the Leu region ($12 > Z > 17$) along simulation time for wild-type BvPIP2;2 (red) and BvPIP2;2L206A (gray). 500-frame running averages are shown as black lines.

twofold increment in the osmotic water permeability of oocytes (Fig. 8A). Similar results have been obtained for the coexpression of BvPIP2;2 and BvPIP1;1 in previous works [30,31]. Also, the $pH_{0.5}$ (6.82 ± 0.02, ±SEM, n = 3) obtained for the coexpression of BvPIP2;2L206A with BvPIP1;1 (Fig. 8C) is similar to the expected for a BvPIP2;2-BvPIP1;1 coexpression. The coexpression of mutant BvPIP2;2L206A with BvPIP1;1 conserved the typical shifting in pH sensing to alkaline values reported for PIP2-PIP1 heterotetramers in comparison with PIP2 homotetramers [30,32]. The only difference found in pH dose–response curves for the coexpression of the mutant and BvPIP1;1 in comparison with the coexpression of wild-type BvPIP2;2 and BvPIP1;1 is the level of inhibition in water transport under acidic conditions, being of approximately 45% for BvPIP2;2L206A-BvPIP1;1 and 97% for BvPIP2;2-BvPIP1;1 (Fig. 8B). These results show that the mutant BvPIP2;2L206A behaves exactly as the wild-type BvPIP2;2 in terms of PIP2-PIP1 interaction but is not able to block water transport efficiently when intracellular pH decreases.

Discussion

In this work, we used a combination of *in silico* and *in vitro* experiments to prove that the dramatic reduction in water transport that occurs after cytosolic acidification in BvPIP2;2 is mainly accounted for the steric hindrance that Leu206 imposes into the channel.

The gating mechanism proposed for all PIP aquaporins emerged from pioneer work done for SoPIP2;1, which open and closed conformation were resolved by X-ray crystallography [10,34]. Here, we show that *B. vulgaris* PIP2;2 is highly similar to SoPIP2;1 in its general structure, but that, in particular, both proteins have the same pore architecture (Figs 1 and 2). This similarity allows us to evaluate the gating mechanism proposed as a general mechanism for the plant PIP family of aquaporins employing a very well-characterized proton-gated PIP2, the BvPIP2;2. Our results show, for the first time to our knowledge, that loopD's leucine residue is an important gate in PIP2 channel being responsible for blocking almost 60% of the water transported when loopD caps the pore (acidic conditions). The constriction generated by Leu206 in BvPIP2;2 pore is lost when this residue is replaced by an Ala (Figs 4 and 6). The simulations show that the replacement of Leu206 for an Ala generates a nearly 50% increment in the average pore radius with a concomitant half reduction in the PMF in the vicinity of this residue. Moreover, the intrinsic osmotic permeability of the mutant channel is increased over threefold in its closed state in comparison with the wild-type (Fig. 4). Interestingly, a similar increment of relative P_f at pH 6.3 (threefold) was found for the *in vitro* experiment when the mutant BvPIP2;2L206A

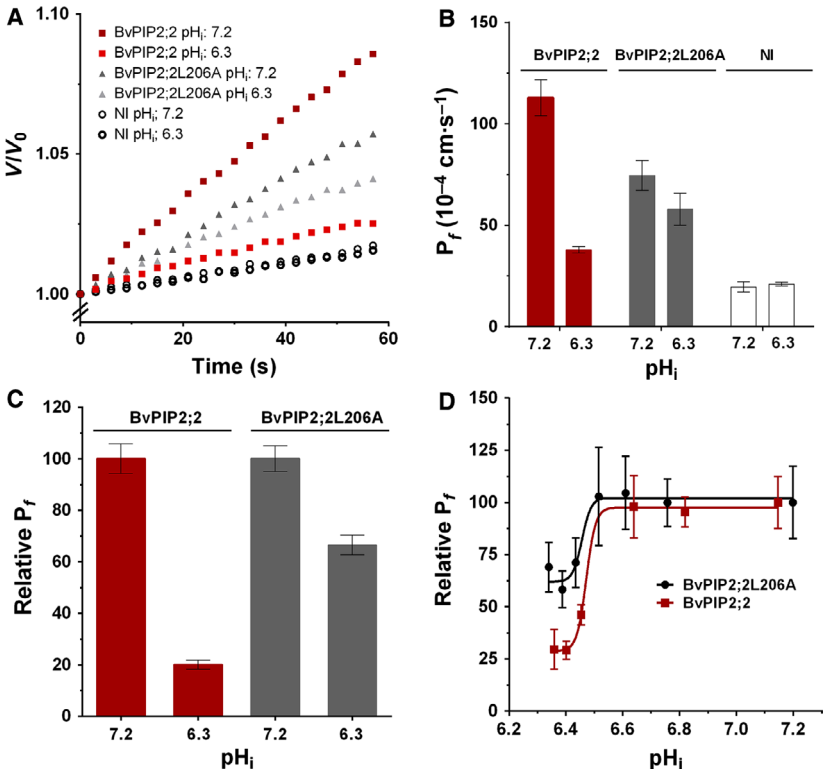

Fig. 7. Osmotic water permeability of wild-type BvPIP2;2 and BvPIP2;2L206A at different cytosolic acidification conditions. (A) Time course evolution of the relative volume change in a single oocyte injected with 7.5 ng of cRNA coding for BvPIP2;2 or BvPIP2;2L206A, both preincubated at different pH acetate solutions and exposed to a hypo-osmotic gradient. NI corresponds to noninjected oocyte (negative control). (B) Mean osmotic water permeabilities of oocytes expressing BvPIP2;2 or BvPIP2;2L206A incubated at different pH acetate solutions corresponding to a typical experiment. (C) Relative P_f obtained analyzing seven (for BvPIP2;2) and eight (for BvPIP2;2L206A) independent experiments, each with 6–15 oocytes for each pH condition. Relative P_f of BvPIP2:2 or BvPIP2:2L206A at pH 6.3 in comparison with pH 7.2 are significantly different ($P < 0.0001$ in both cases). The relative P_f of BvPIP2:2 or BvPIP2:2L206A at pH 6.3 are significantly different ($P < 0.0001$). (D) pH dose–response curves of the plasma membrane P_f of oocytes expressing wild-type BvPIP2;2 (red squares) or mutant BvPIP2;2L206A (black dots), $n = 7–17$ oocytes tested in one representative experiment among three (for BvPIP2;2L206A) or 2 (for BvPIP2;2) replicates with similar results. Continuous lines are the graphical representation a sigmoidal function fitted to the experimental data. Values in B, C, and D are shown as mean ± SEM.

is expressed in Xenopus oocytes (Fig. 7C). This increment in water transport is due to the loss of the hindrance generated by the protrusion of Leu206 side chain. The residual inhibition that is detected in the mutant at acidic conditions can be due to other residues lining the pore in the vicinity of Leu206. It was suggested that in SoPIP2;1, Leu197 can act together with His99, Val104, Leu108, Pro195, and Val194 to block the water transport [10]. Khandelia *et al.* [40] proved that virtual truncation of loopD in SoPIP2;1 removing Pro195 and Val194 residues increase water transport. However, this truncation also disrupted the bonding network between the loopD and the N-terminal tail. Here, we rule out any other kind of structural modification of the channel as a possible cause of the improved water permeability after leucine replacement by alanine. On one hand, loopD network interaction with N-terminal tail is not altered in the mutant, conserving the closed conformation of the channel (Fig. 5, data from *in silico* experiments) and on the other hand, cooperativity and $pH_{0.5}$, parameters that depends on structural contacts in the whole molecule, are similar in the mutant and wild-type channel (Fig. 7, data from *in vitro* experiments).

The leucine gate studied here can be triggered by cytosolic acidification both in BvPIP2;2 homotetramers and BvPIP2;2–BvPIP1;1 heterotetramers. The heterotetramerization among the PIP1 and PIP2 paralogues is a distinguished phenomenon of the PIP aquaporin subfamily [41,42]. It is known that the assembly of PIP2 and PIP1 protomers occurs with random stoichiometry [31,32,43] and that their precise interactions are controlled by specific promoter contacts [43,44]. The pH response of homotetramers and heterotetramers has been well characterized for BvPIP and it is known that water transport is higher and $pH_{0.5}$ is shifted to more alkaline values for PIP2-PIP1 heterotetramers in comparison with PIP2 homotetramers [30–32,41]. The only feature preserved in both heterotetramers and PIP2 homotetramers is the degree of cooperativity for pH sensing [31,35]. In our experiments, it is clear that interaction interfaces of the BvPIP2L206A channel are not altered by the mutation since its coexpression with BvPIP1;1 presents the

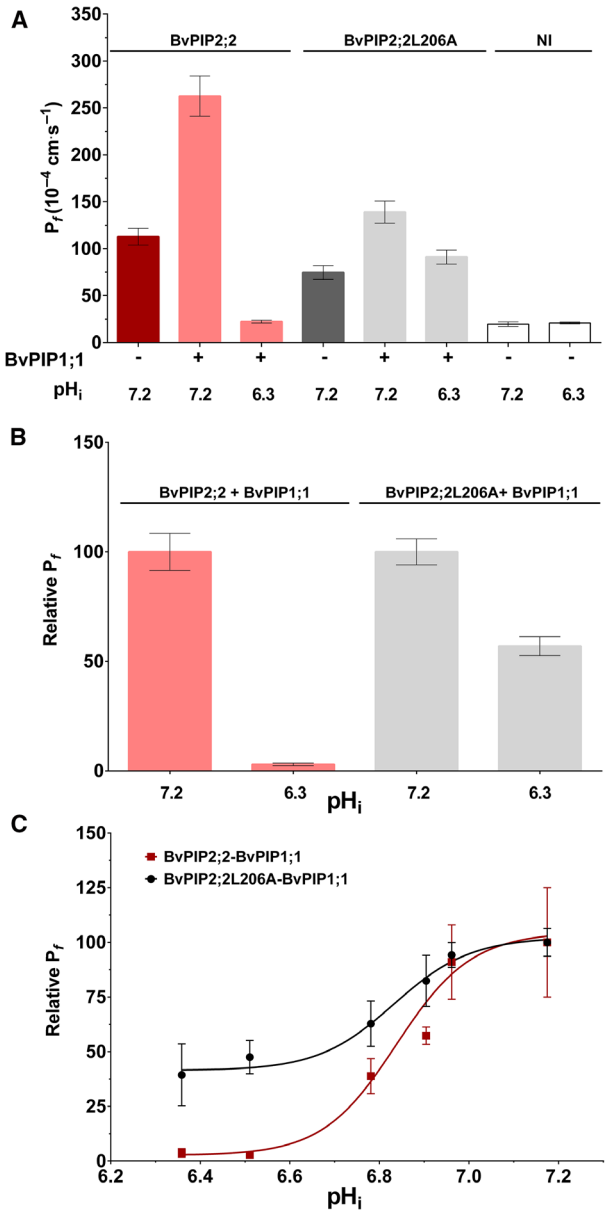

Fig. 8. P_f dependence on oocyte internal pH for the coexpression of BvPIP2;2L206A and BvPIP1;1. (A) Mean osmotic water permeabilities of oocytes expressing BvPIP2;2, BvPIP2;2- BvPIP1;1, BvPIP2;2L206A, BvPIP2;2L206A, or BvPIP2;2L206A-BvPIP1;1, all incubated at different pH acetate solutions and exposed to a hypo-osmotic gradient. NI is noninjected oocytes (negative control). Values are mean ± SEM, n = 7–14 oocytes. This is one representative experiment of three replicates. (B) Relative P_f obtained analyzing three (for BvPIP2;2-BvPIP1;1) and five (for BvPIP2;2L206A-BvPIP1;1) independent experiments. Relative P_f of BvPIP2:2-BvPIP1;1 or BvPIP2:2L206A-BvPIP1;1 at pH 6.3 in comparison with pH 7.2 are significantly different ($P < 0.0001$ in both cases). The relative P_f of BvPIP2:2-BvPIP1;1 or BvPIP2:2L206A-BvPIP1;1 at pH 6.3 are significantly different ($P < 0.0001$). (C) Relative P_f behavior after cytosolic acidification tested in oocytes coinjected with BvPIP2;2L206A-BvPIP1;1 (7.5 ng of each cRNA per oocyte) or BvPIP2;2-BvPIP1;1 (7.5 ng of each cRNA per oocyte) used as control. The data points are representative values obtained from the same batch of oocytes (mean Relative P_f ± SEM). This is one representative experiment of three independent experiments, 4–14 oocytes were tested for each condition in each replicate.

typical characteristics of the PIP heterotetramers vs. homotetramers: higher water transport, shifted $pH_{0.5}$ to alkaline values, and conserved sigmoidicity (Fig. 8). However, the inhibition in water transport by acidification is affected for the coexpression, showing that Leu206 is relevant in BvPIP2;2 pore gating not only when this molecule is assembled as a homotetramer but also as a heterotetramer with BvPIP1;1 (Fig. 8). Peculiarly, the inhibition found for the BvPIP2;2L206A-BvPIP1;1 coexpression is similar to the one found in the homotetrameric mutant. This result is intriguing since in the homoterameric mutant the four monomers have the replacement of Leu206 for an Ala while in the heterotetramer, BvPIP1;1 conserves its loopD's Leu. A speculation about the impact of the interaction in the conformation of the water pore cannot straightforwardly be done since the pH dose–response curve of BvPIP1;1 homotetramers is unknown as there are still no solved structures for the PIP1 homotetramers nor for the PIP2-PIP1 heterotetramers. However, since it was reported that the pores of both PIP2 and PIP1 are altered after their interaction [32,44–46], it is plausible that also the gating mechanisms were altered.

Taken together, all results reported here show that Leu206 conforms a relevant gate, located at the cytoplasmic entry of the channel for pH inhibition of water transport in PIP aquaporins. All aquaporins showed a constriction site defined by the Ar/R selectivity filter located in the extracellular entry of the protein, but gated aquaporins have been shown to have a second constriction site at the cytoplasmic side of the channel. This second constriction is characterized by the protrusion of a single residue into the pore that consequently interrupts the single file of water molecules, as Leu206 does here. In Aqy1 this single-residue gate is realized by Tyr31 [47]. This residue is located in the N terminus of Aqy1 but occupies, in the tertiary structure of the channel, the same location as Leu206 in BvPIP2;2 [47,48]. Mechanosensitivity and phosphorylation of Ser107 in loopB, seem to be the triggering factors controlling Aqy1 gating by Tyr31 [47,49]. AQP0 has also been reported as a gated aquaporin and the residue proposed as gate in the cytoplasmic entry of the channel is Tyr149, located in loopB [50]. AQP0's Tyr149 also occupies a position equivalent to loopD's Leu in PIP2 [10]. The replacement of Tyr149 regulates not only the water permeability in AQP0 but also its calcium modulation [51,52]. It is well know that Ca^{2+}-calmodulin controls AQP0 activity by calmodulin binding to two neighboring C-terminal tails, and it was shown that the probability of the cytoplasmic constriction adopting a closed state increases in the presence of calmodulin [51]. Recently, it was proposed that also HsAQP5, HsAQP4, and HsAQP10 present a cytoplasmic gating mechanism based on only one key gate residue, being the blocking key residues His67 [53], His95 [23,54], and His80 [55], respectively. Again, these histidine residues are located at the cytoplasmic entry of those aquaporins. Interestingly, in HsAQP10, the acidification opens the channel to increase glycerol transport [55]. In the cases of HsAQP5 and HsAQP4, the knowledge about the gating mechanisms are not as clear as in the other cases, such as the reported here for PIP2, where the movement of an important flexible domain of the proteins jointly activates the single-residue gate.

Can the nature of the leucine gate be hydrophobic or is it purely steric? Hydrophobic gating is a well-proved phenomenon that was originally proposed for ion channels and refers to the dewetting of some region of the channel pore that renders a low ionic permeability. Indeed, this concept was used to describe those channel structures where 'the gate is formed by a ring of hydrophobic side chains that do not physically occlude the pore' [56]. In narrow hydrophobic regions (radius ≤ 4 Å) a pore will spontaneously be dewetted and thus the channel presents a closed state. Several channels present this kind of gating mechanism by dewetting, that is, a decrease in the number of water molecules in a particular region of the pore is the main effect of hydrophobic gating. For example, the nature of the gate in GLIC and ELIC channels has been shown to be hydrophobic [57]. However, it is not clear that these cases are similar to aquaporins, whose pores' radii are always narrower than ion channel pores and water is transported through a single file mechanism. From our experiments, the modification of Leu206 side chain was sufficient to allow a higher water permeability, even when pore radius is still narrower in comparison with the radius reported for ion channel hydrophobic gating. Thus, in the case of PIP2 it seems that the elimination of the steric constriction is the factor that allowed a higher water permeability. Then, we consider that the nature of the PIP leucine gate is mainly steric. Notwithstanding, as pointed by Zhu and Hammer [57], there may not always be a clear boundary between the regimes of steric and hydrophobic gating associated with the intrinsic dynamic of channel's pores due to thermal fluctuations together with the flexibility of protein structures.

There is unambiguous evidence from functional data [18–20,29–,32] and X-ray crystallography [10,16,34] showing that PIP aquaporins are proton-gated channels, however, the mechanisms that effectively operate after loopD capping to control water

transport through the PIP pore have been kept as an structural hypothesis until now. The mechanism that close PIP pore is of huge physiological relevance, indeed, one of the early responses of plants under anoxia by flooding is the downregulation of water uptake by the coordinate inhibition of plant PIP aquaporins [19]. The present work demonstrates that the proposed leucine gate acting at the cytoplasmic entry of PIP2 channel is effectively a crucial steric gate controlling water transport in this aquaporin subfamily.

Methods

Sequence analysis

Beta vulgaris plasma membrane intrinsic proteins, BvPIP2;2 (GQ227846.1) and *S. oleracea* SoPIP2;1 (Q41372) were compared. To obtain the conserved loopD sequence, a search was performed with BLASTP tool (http://blast.ncbi.nlm.nih.gov/Blast.cgi) using BvPIP2;2 as input. Ninety-six sequences were selected to perform multiple sequence alignment (MSA). All MSAs were done with CLUSTAL OMEGA [58]. The logo was performed using WebLogo (http://weblogo.berkeley.edu/logo.cgi) to generate a graphical representation of the patterns within the MSA.

Molecular dynamics simulation and data analysis

Molecular mechanic simulations were performed for homotetrameric assemblies using SoPIP2;1 in a closed state crystal 3D structure obtained from the Protein Data Bank (1Z98) [10] and BvPIP2;2 homology models obtained through the Swiss model homology-modeling server [59], using 1Z98 crystal as a template. Crystallographic water molecules were removed and Cd^{2+} ions were replaced by Ca^{2+}. The selected template corresponds to the SoPIP2;1 closed state at pH 8 obtained instead of 4IA4, which also corresponds to SoPIP2;1 closed but at pH 6 since this template has a lower resolution (3.1 Å) and the author reports that the structures obtained at both pH are not significantly different [34]. All the homotetrameric assemblies were embedded in a fully hydrated 180 × 180 Å POPC bilayer using the membrane builder tool provided in the CHARMM-GUI website [60–63]. Approximately 75 000 explicit water molecules of the TIP3P water model [64] and near 195 sodium and chloride ions were added to achieve a concentration of 150 mM. Total box dimensions in all simulations were approximately 180 × 180 × 115 Å ($X \times Y \times Z$). A minimization stage was performed prior to the heating stages. The system was first heated from 0 to 100 K with all the lipids under weak harmonic constraints and then heated from 100 to 303 K with an anisotropic Berendsen weak-coupling barostat to equilibrate the pressure, under the same harmonic constraints. Thereafter, constrain-free molecular dynamics was run in an NPT ensemble with full periodic boundary conditions. Nonbonded interactions (electrostatic and Lennard-Jones) were simulated with a cutoff of 10 Å. Electrostatic interactions were simulated using Particle Mesh Ewald for long range interactions. All simulations were performed using AMBER 16 MD simulations package and parameters form AMBER14SB and LIPID14 force fields [65–67]. Covalent hydrogen bonds were constrained using SHAKE algorithm, allowing a time step of 2 fs. The simulations were performed at a temperature of 303 K using a Langevin thermostat and pressure were kept at 1 bar by an anisotropic Berendsen barostat. Equilibrium simulations of 520 ns were carried out for SoPIP2;1, BvPIP2;2, and BvPIP2;2L206A homology models. The protein structures extend from residue 24–274 in those for *S. oleracea* and from residue 26–289 in the case of *B. vulgaris* models. The first 20 ns of each trajectory were discarded since the area per lipid stabilized after the first 5 ns. We assumed independent behavior for each monomer that allowed us to treat datasets extracted from each monomer as independent samples. HOLE module of MDANALYSIS package and an in-house R script was used to calculate pore dimensions in the Z axis for each trajectory and statistical processing, respectively [68–70]. The intrinsic osmotic permeability (p_f) was extracted from 10 equilibrium simulations (10 ns long) using 10 frames along the 500-ns simulations (one every 50 ns) as initial coordinates. Calculations were carried out with an in-house R script as described for the collective diffusion method by Zhu: MSD in the Z axis was measured for the water molecules occupying each pore in each single simulation [71]. Hydrogen bonds data were extracted from the 500-ns equilibrium simulations and geometrical properties were measured employing analysis tool included in the AMBERTOOLS package.

DNA constructions

Beta vulgaris plasma membrane intrinsic proteins, BvPIP2;2 (GQ227846.1) and BvPIP1,1 (GQ227845.1), were cloned into BglII and SpeI sites of a pT7Ts-derived vector containing T7 RNA polymerase promoter and carrying the 5′ and 3′ translated regions of the *X. laevis* β globin gene. Mutated cDNA encoding BvPIP2;2L206A was obtained by site-directed mutagenesis using custom-made oligonucleotides primers (Genbiotech, Buenos Aires, Argentina). Primers used to mutate a leucine to alanine (L206A) in BvPIP2;2 are 5′-ggtaggggtgccgctacaggaacatgggaatccct-3′ and 5′-agggattcccatgttcctgtagcggcacccctacc-3′.

The mutation reaction was performed by site-directed mutagenesis PCR using Phusion High-Fidelity DNA Polymerase (New England Biolabs, Ipswich, MA, USA). DNA sequencing (Macrogen Inc., Seol, Korea) was used to corroborate all sequences.

In vitro RNA synthesis

The capped cRNA encoding for BvPIP1;1 and BvPIP2;2 were synthesized *in vitro* using the mMESSAGE mMACHINE T7 High Yield Capped RNA Transcription Kit (Ambion, Austin, TX, USA), and BvPIP2:2L206A with mMESSAGE mMACHINE T7 High Yield Capped RNA ULTRA Transcription Kit (Ambion, Austin, TX, USA) and mMESSAGE mMACHINE T7 High Yield Capped RNA Transcription Kit (Ambion), as described previously [72]. The synthesized products were suspended in RNAase-free water and stored at −20 °C until use. Agarose gel electrophoresis and GelRed (BioAmerica Biotech Inc., Miami, FL, USA) staining were used to check the absence of unincorporated nucleotides in the cRNA after every *in vitro* cRNA synthesis. The cRNA was quantified in a Bio-Tek PowerWave™ Microplate Spectrophotometer (Fisher Scientific, Lenexa, KS, USA).

Oocyte water transport assays

Defolliculated stage V–VI *X. laevis* oocytes were microinjected with cRNA coding for different PIP and incubated for 3 or 4 days in ND96 buffer (96 mM NaCl, 2 mM KCl, 1 mM $MgCl_2$, 1.8 mM $CaCl_2$, and 5 mM HEPES pH 7.5; ~ 200 mOsmol·kg^{-1} H_2O) at 18 °C prior to performing the experiments. The osmotic water permeability (P_f) of oocytes injected or noninjected with cRNA was determined by measuring the rate of oocyte swelling, as explained before [30]. Briefly, P_f was determined by measuring the rate of oocyte swelling induced in response to fivefold dilution of the ND96 buffer with distilled water. Changes in oocyte volume were video-monitored by a WB-99 color video camera (1.3 MP; Panacom, Buenos Aires, Argentina) attached to a zoom stereo-microscope (Leica L2; Leica, Wetzlar, Germany). Cell swelling was video-captured in still images using the AMCAP version 9.20 (http://noeld.com/programs.asp?cat=video) and then the images were analyzed by treating each oocyte image as a growing sphere whose volume could be inferred from its cross-sectional area (software IMAGE J version 1.37, https://imagej.nih.gov/ij/index.html, NIH, Bethesda, MD, USA). P_f was calculated according to [73], $P_f = V_o\ [d(V/V_o)/dt]/[S\ V_w\ (Osm_{in} - Osm_{out})]$, where V_o is initial oocyte volume (9×10^{-4} cm^3), V/V_o is the relative volume, S is the surface area of the oocyte (0.045 cm^2), V_w the molecular volume of water (18 cm^3·mol^{-1}) and $Osm_{in} - Osm_{out}$ the osmotic driving force. Noninjected oocytes were used as negative controls. All osmolarities were measured in vapor pressure osmometer (5600C Wescor Inc., Logan, UT, USA).

pH modulation of oocyte water transport

For pH inhibition experiments the internal proton concentration of oocytes was modified following an already described protocol [19,30]. Briefly, the internal pH of oocytes was acidified by preincubating them for 20 min in different pH acetate solutions (50 mM sodium actate, 20 mM MES for the 5.8–6.8 pH interval or HEPES for the 7.0–7.5 pH interval), supplemented with 1 M mannitol until the desired osmolarity was achieved (200 ± 5 mOsmol·kg^{-1} H_2O). The internal pH was calculated following the calibration performed in Ref. [30]. The swelling response was induced by transferring the oocytes to a dilution of the incubation solution with distilled water. The relative P_f was obtained by the equation: Relative $P_f = [(P_f\ pH\ 6.3 - P_f\ NI)/(P_f\ pH\ 7.2 - P_f\ NI)] \times 100$. NI stands for noninjected oocytes used as negative control. Relative P_f values are used to discard any possible difference in the translating rate or membrane insertion rate among the mutant and the wild-type channels that can induced to misinterpretation of functional data. Lower plasma membrane insertion was previously reported for mutant AQP [74].

For pH dose–response curves an empirical sigmoidal function (Eqn) was fitted to the experimental data by nonlinear regression procedure (implemented in GraphPad Prism Inc., San Diego, CA, USA):()

$$P_f = P_{f\min} + (P_{f\max} - P_{f\min})\frac{K_{0.5}^{n_H}}{K_{0.5}^{n_H} + [H^+]^{n_H}},$$

where $P_{f\max}$ and $P_{f\min}$ are the asymptotic maximal and minimal values of the oocyte water permeability (P_f), $K_{0.5}^{n_H}$ is the $[H^+]$ at which the water permeability change is half maximal, and n_H is an empirical coefficient giving account of the mismatch respect to the hyperbolic behavior. Parameter $pH_{0.5}$ is defined as $pH_{0.5} \equiv -\log(K_{0.5})$.

Statistics

Significant differences between groups were calculated using a two-tailed Student *t* test.

Acknowledgements

We thank F. Luis González Flecha, G. Soto, and N. Ayub for their critical discussions. This work was supported by ANPCYT (PICT 2017-0244 to KA, PICT 2015-2761 to DAE), UBA (UBACYT 2002017010017 8BA01 to KA and UBACYT 20020120300025B to DAE), and UNHAUR (PIUNHAUR-5 2018 to GZDP). AZ acknowledges Agencia Nacional de Investigación e Innovación (ANII) Uruguay for postdoctoral fellowship funding.

Conflict of interest

The authors declare no conflict of interest.

Author contributions

KA, ACF, GZDP, AZ, and DAE planned experiments; ACF, GZDP, and VV performed experiments; KA, ACF, GZDP, LAC, LA, AZ, and DAE analyzed data; KA, ACF, GZP, LAC, and LA prepared the figures; KA wrote the manuscript; all authors read and edited the manuscript.

References

1 Agre P (2006) The aquaporin water channels. *Proc Am Thorac Soc* **3**, 5–13.
2 Fujiyoshi Y, Mitsuoka K, de Groot BL, Philippsen A, Grubmüller H, Agre P & Engel A (2002) Structure and function of water channels. *Curr Opin Struct Biol* **12**, 509–515.
3 Anderberg HI, Kjellbom P & Johanson U (2012) Annotation of *Selaginella moellendorffii* major intrinsic proteins and the evolution of the protein family in terrestrial plants. *Front Plant Sci* **3**, 33.
4 Chaumont F & Tyerman SD (2014) Aquaporins: highly regulated channels controlling plant water relations. *Plant Physiol* **164**, 1600–1618.
5 Maurel C, Boursiac Y, Luu D, Santoni V, Shahzad Z & Verdoucq L (2015) Aquaporins in plants. *Physiol Rev* **95**, 1321–1358.
6 Murata K, Mitsuoka K, Hirai T, Walz T, Agre P, Heymann JB, Engel A & Fujiyoshi Y (2000) Structural determinants of water permeation through aquaporin-1. *Nature* **407**, 599–605.
7 Sui H, Han BG, Lee JK, Walian P & Jap BK (2001) Structural basis of water-specific transport through the AQP1 water channel. *Nature* **414**, 872–878.
8 Fu D, Libson A, Miercke LJ, Weitzman C, Nollert P, Krucinski J & Stroud RM (2000) Structure of a glycerol-conducting channel and the basis for its selectivity. *Science* **290**, 481–486.
9 Harries WEC, Akhavan D, Miercke LJW, Khademi S & Stroud RM (2004) The channel architecture of aquaporin 0 at a 2.2-A resolution. *Proc Natl Acad Sci USA* **101**, 14045–14050.
10 Törnroth-Horsefield S, Wang Y, Hedfalk K, Johanson U, Karlsson M, Tajkhorshid E, Neutze R & Kjellbom P (2006) Structural mechanism of plant aquaporin gating. *Nature* **439**, 688–694.
11 Newby ZER, O'Connell J III, Robles-Colmenares Y, Khademi S, Miercke LJ & Stroud RM (2008) Crystal structure of the aquaglyceroporin PfAQP from the malarial parasite *Plasmodium falciparum*. *Nat Struct Mol Biol* **15**, 619–625.
12 Frick A, Eriksson UK, de Mattia F, Oberg F, Hedfalk K, Neutze R, de Grip WJ, Deen PMT & Törnroth-Horsefield S (2014) X-ray structure of human aquaporin 2 and its implications for nephrogenic diabetes insipidus and trafficking. *Proc Natl Acad Sci USA* **111**, 6305–6310.
13 Kirscht A, Kaptan S, Bienert G, Chaumont F, Nissen P, De Groot D, Kjellbom P, Gourdon P & Johanson U (2016) Crystal structure of an ammonia-permeable aquaporin. *PLoS Biol* **14**, e1002411.
14 Preston GM, Jung JS, Guggino WB & Agre P (1994) Membrane topology of aquaporin CHIP. Analysis of functional epitope-scanning mutants by vectorial proteolysis. *J Biol Chem* **269**, 1668–1673.
15 Hedfalk K, Törnroth-Horsefield S, Nyblom M, Johanson U, Kjellbom P & Neutze R (2006) Aquaporin gating. *Curr Opin Struct Biol* **16**, 447–456.
16 Nyblom M, Frick A, Wang Y, Ekvall M, Hallgren K, Hedfalk K, Neutze R, Tajkhorshid E & Törnroth-Horsefield S (2009) Structural and functional analysis of SoPIP2;1 mutants adds insight into plant aquaporin gating. *J Mol Biol* **387**, 653–668.
17 Fischer M & Kaldenhoff R (2008) On the pH regulation of plant aquaporins. *J Biol Chem* **283**, 33889–33892.
18 Gerbeau P, Amodeo G, Henzler T, Santoni V, Ripoche P & Maurel C (2002) The water permeability of *Arabidopsis* plasma membrane is regulated by divalent cations and pH. *Plant J* **30**, 71–81.
19 Tournaire-Roux C, Sutka M, Javot H, Gout E, Gerbeau P, Luu DTD-T, Bligny R & Maurel C (2003) Cytosolic pH regulates root water transport during anoxic stress through gating of aquaporins. *Nature* **425**, 393–397.
20 Alleva K, Niemietz CM, Sutka M, Maurel C, Parisi M, Tyerman SD & Amodeo G (2006) Plasma membrane of *Beta vulgaris* storage root shows high water channel activity regulated by cytoplasmic pH and a dual range of calcium concentrations. *J Exp Bot* **57**, 609–621.
21 Verdoucq L, Grondin A & Maurel C (2008) Structure-function analysis of plant aquaporin AtPIP2;1 gating by divalent cations and protons. *Biochem J* **415**, 409–416.
22 Johansson I, Karlsson M, Shukla VK, Chrispeels MJ, Larsson C & Kjellbom P (1998) Water transport activity of the plasma membrane aquaporin PM28A is regulated by phosphorylation. *Plant Cell* **10**, 451–459.
23 Kaptan S, Assentoft M, Schneider HP, Fenton RA, Deitmer JW, MacAulay N & De Groot BL (2015) H95 is a pH-dependent gate in aquaporin 4. *Structure* **23**, 2309–2318.
24 Mósca A, de Almeida A, Wragg D, Martins A, Sabir F, Leoni S, Moura T, Prista C, Casini A & Soveral G (2018) Molecular basis of aquaporin-7 permeability regulation by pH. *Cells* **7**, 207.
25 Soto G, Fox R, Ayub N, Alleva K, Guaimas F, Erijman EJ, Mazzella A, Amodeo G & Muschietti J (2010) TIP5;1 is an aquaporin specifically targeted to pollen mitochondria and is likely involved in nitrogen

remobilization in *Arabidopsis thaliana*. *Plant J* **64**, 1038–1047.
26 Leitão L, Prista C, Moura TF, Loureiro-Dias MC & Soveral G (2012) Grapevine aquaporins: gating of a tonoplast intrinsic protein (TIP2;1) by cytosolic pH. *PLoS One* **7**, e33219.
27 Rodrigues C, Mósca AF, Martins AP, Nobre T, Prista C, Antunes F, Gasparovic AC & Soveral G (2016) Rat aquaporin-5 is pH-gated induced by phosphorylation and is implicated in oxidative stress. *Int J Mol Sci* **17**, 2090.
28 Zeuthen T & Klaerke DA (1999) Transport of water and glycerol in aquaporin 3 is gated by H(+). *J Biol Chem* **274**, 21631–21636.
29 Alleva K, Marquez M, Villarreal N, Mut P, Bustamante C, Bellati J, Martínez G, Civello M & Amodeo G (2010) Cloning, functional characterization, and co-expression studies of a novel aquaporin (FaPIP2;1) of strawberry fruit. *J Exp Bot* **61**, 3935–3945.
30 Bellati J, Alleva K, Soto G, Vitali V, Jozefkowicz C & Amodeo G (2010) Intracellular pH sensing is altered by plasma membrane PIP aquaporin co-expression. *Plant Mol Biol* **74**, 105–118.
31 Jozefkowicz C, Sigaut L, Scochera F, Soto G, Ayub N, Pietrasanta LI, Amodeo G & González Flecha FL (2016) PIP water transport and its pH dependence are regulated by tetramer stoichiometry. *Biophys J* **110**, 1312–1321.
32 Yaneff A, Sigaut L, Marquez M, Alleva K, Pietrasanta LI & Amodeo G (2014) Heteromerization of PIP aquaporins affects their intrinsic permeability. *Proc Natl Acad Sci USA* **111**, 231–236.
33 Shelden MC, Howitt SM, Kaiser BN & Tyerman SD (2009) Identification and functional characterisation of aquaporins in the grapevine, *Vitis vinifera*. *Funct Plant Biol* **36**, 1065–1078.
34 Frick A, Järvå M & Törnroth-Horsefiel S (2013) Structural basis for pH gating of plant aquaporins. *FEBS Lett* **587**, 989–993.
35 Vitali V, Jozefkowicz C, Canessa Fortuna A, Soto G, González Flecha FL & Alleva K (2019) Cooperativity in proton sensing by PIP aquaporins. *FEBS J* **286**, 991–1002.
36 Horsefield R, Norden K, Fellert M, Backmark A, Tornroth-Horsefield S, Terwisscha van Scheltinga AC, Kvassman J, Kjellbom P, Johanson U & Neutze R (2008) High-resolution x-ray structure of human aquaporin 5. *Proc Natl Acad Sci USA* **105**, 13327–13332.
37 Horner A, Zocher F, Preiner J, Ollinger N, Siligan C, Akimov SA & Pohl P (2015) The mobility of single-file water molecules is governed by the number of H-bonds they may form with channel-lining residues. *Sci Adv* **1**, 1–6.
38 Xin L, Su H, Nielsen CH, Tang C, Torres J & Mu Y (2011) Water permeation dynamics of AqpZ: a tale of two states. *Biochim Biophys Acta* **1808**, 1581–1586.
39 Zhu F, Tajkhorshid E & Schulten K (2004) Theory and simulation of water permeation in aquaporin-1. *Biophys J* **86**, 50–57.
40 Khandelia H, Jensen MOØ & Mouritsen OG (2009) To gate or not to gate: using molecular dynamics simulations to morph gated plant aquaporins into constitutively open conformations. *J Phys Chem B* **113**, 5239–5244.
41 Fetter K, Van Wilder V, Moshelion M & Chaumont F (2004) Interactions between plasma membrane aquaporins modulate their water channel activity. *Plant Cell* **16**, 215–228.
42 Jozefkowicz C, Berny MC, Chaumont F & Alleva K (2017) Heteromerization of plant aquaporins. In Plant Aquaporins, From Transport to Signalling (Chaumont F & Tyerman S, eds), pp. 29–46. Springer, Berlin.
43 Berny MC, Gilis D, Rooman M & Chaumont F (2016) Single mutations in the transmembrane domains of maize plasma membrane aquaporins affect the activity of monomers within a heterotetramer. *Mol Plant* **9**, 986–1003.
44 Vajpai M, Mukherjee M & Sankararamakrishnan R (2018) Cooperativity in plant plasma membrane intrinsic proteins (PIPs): mechanism of increased water transport in maize PIP1 channels in hetero-tetramers. *Sci Rep* **8**, 12055.
45 Otto B, Uehlein N, Sdorra S, Fischer M, Ayaz M, Belastegui-Macadam X, Heckwolf M, Lachnit M, Pede N, Priem N *et al.* (2010) Aquaporin tetramer composition modifies the function of tobacco aquaporins. *J Biol Chem* **285**, 31253–31260.
46 Byrt CS, Zhao M, Kourghi M, Bose J, Henderson SW, Qiu J, Gilliham M, Schultz C, Schwarz M, Ramesh SA *et al.* (2016) Non-selective cation channel activity of aquaporin AtPIP2;1 regulated by Ca2+ and pH. *Plant, Cell Environ* **40**, 802–815.
47 Fischer G, Kosinska-Eriksson U, Aponte-Santamaría C, Palmgren M, Geijer C, Hedfalk K, Hohmann S, de Groot BL, Neutze R & Lindkvist-Petersson K (2009) Crystal structure of a yeast aquaporin at 1.15 angstrom reveals a novel gating mechanism. *PLoS Biol* **7**, e1000130.
48 Aponte-Santamaría C, Fischer G, Bath P, Neutze R & De Groot BL (2017) Temperature dependence of protein-water interactions in a gated yeast aquaporin. *Sci Rep* **7**, 1–14.
49 Nyblom M & Tornroth-Horsefield S (2016) Regulation of eukaryotic aquaporins. In Aquaporins in Health and Disease: New Molecular Targets for Drug Discovery (Graca S, Nielsen S & Casini A, eds), pp. 53–76. CRC Press, Taylor & Francis Group, Boca Raton, FL.

50 Gonen T, Sliz P, Kistler J, Cheng Y & Walz T (2004) Aquaporin-0 membrane junctions reveal the structure of a closed water pore. *Nature* **429**, 193–197.

51 Reichow SL, Clemens DM, Freites JA, Németh-Cahalan KL, Heyden M, Tobias DJ, Hall JE & Gonen T (2013) Allosteric mechanism of water-channel gating by Ca2+–calmodulin. *Nat Struct Mol Biol* **20**, 1085–1092.

52 Saboe PO, Rapisarda C, Kaptan S, Hsiao YS, Summers SR, De Zorzi R, Dukovski D, Yu J, de Groot BL, Kumar M *et al.* (2017) Role of pore-lining residues in defining the rate of water conduction by aquaporin-0. *Biophys J* **112**, 953–965.

53 Janosi L & Ceccarelli M (2013) The gating mechanism of the human aquaporin 5 revealed by molecular dynamics simulations. *PLoS One* **8**, e59897.

54 Alberga D, Nicolotti O, Lattanzi G, Nicchia GP, Frigeri A, Pisani F, Benfenati V & Mangiatordi GF (2014) A new gating site in human aquaporin-4: insights from molecular dynamics simulations. *Biochim Biophys Acta* **1838**, 3052–3060.

55 Gotfryd K, Mósca AF, Missel JW & Truelsen SF (2018) Human adipose glycerol flux is regulated by a pH gate in AQP10. *Nat Commun* **9**, 47–49.

56 Beckstein O, Biggin PC & Sansom MSP (2001) A hydrophobic gating mechanism for nanopores. *J Phys Chem B* **105**, 12902–12905.

57 Zhu F & Hummer G (2012) Drying transition in the hydrophobic gate of the GLIC channel blocks ion conduction. *Biophys J* **103**, 219–227.

58 Sievers F, Wilm A, Dineen D, Gibson TJ, Karplus K, Li W, Lopez R, McWilliam H, Remmert M, Söding J *et al.* (2011) Fast, scalable generation of high-quality protein multiple sequence alignments using Clustal Omega. *Mol Syst Biol* **7**, 539.

59 Waterhouse A, Bertoni M, Bienert S, Studer G, Tauriello G, Gumienny R, Heer FT, De Beer TAP, Rempfer C, Bordoli L *et al.* (2018) SWISS-MODEL: homology modelling of protein structures and complexes. *Nucleic Acids Res* **46**, 296–303.

60 Jo S, Kim T, Iyer WG & Im W (2008) CHARMM-GUI: a web-based graphical user interface for CHARMM. *J Comput Chem* **29**, 1859–1865.

61 Wu EL, Cheng X, Jo S, Rui H, Song KC, Dávila-Contreras EM, Qi Y, Lee J, Monje-Galvan V, Venable RM *et al.* (2014) CHARMM-GUI membrane builder toward realistic biological membrane simulations. *J Comput Chem* **35**, 1997–2004.

62 Jo S, Lim JB, Klauda JB & Im W (2009) CHARMM-GUI membrane builder for mixed bilayers and its application to yeast membranes. *Biophys J* **97**, 50–58.

63 Jo S, Kim T & Im W (2007) Automated builder and database of protein/membrane complexes for molecular dynamics simulations. *PLoS One* **2**, e880.

64 Jorgensen WL, Chandrasekhar J, Madura JD, Impey RW & Klein ML (1983) Comparison of simple potential functions for simulating liquid water. *J Chem Phys* **79**, 461–470.

65 Case D, Babin V, Berryman J, Betz R, Cai Q, Cerutti D, Cheatham T, Darden T, Duke R, Gohlke H *et al.* (2014) AMBER 14. University of California, San Francisco, CA.

66 Case DA, Betz RM, Cerutti DS, Cheatham TE III, Darden TA, Duke RE, Giese TJ, Gohlke H, Goetz AW, Homeyer N *et al.* (2016) AMBER 16. University of California, San Francisco, CA.

67 Maier JA, Martinez C, Kasavajhala K, Wickstrom L, Hauser K & Simmerling C (2015) ff14SB : improving the accuracy of protein side chain and backbone parameters from ff99SB. *J Chem Theory Comput* **11**, 3696–3713.

68 Gowers R, Linke M, Barnoud J, Reddy T, Melo M, Seyler S, Domański J, Dotson D, Buchoux S, Kenney I *et al.* (2016) MDAnalysis: a Python package for the rapid analysis of molecular dynamics simulations. In Proceedings of the 15th Python in Science Conference (Benthall S & Rostrup S, eds), pp. 98–105. Austin, TX. http://conference.scipy.org/proceedings/scipy2016/

69 Michaud-Agrawal N, Denning EJ, Woolf TB & Beckstein O (2011) MDAnalysis: a toolkit for the analysis of molecular dynamics simulations. *J Comput Chem* **32**, 2319–2327.

70 Smart OS, Neduvelil JG, Wang X, Wallace BA & Sansom MSP (1996) HOLE: a program for the analysis of the pore dimensions of ion channel structural models. *J Mol Graph* **14**, 354–360.

71 Zhu F, Tajkhorshid E & Schulten K (2004) Collective diffusion model for water permeation through microscopic channels. *Phys Rev Lett* **93**, 1–4.

72 Jozefkowicz C, Rosi P, Sigaut L, Soto G, Pietrasanta LI, Amodeo G & Alleva K (2013) Loop A is critical for the functional interaction of two *Beta vulgaris* PIP aquaporins. *PLoS One* **8**, e57993.

73 Zhang RB & Verkman AS (1991) Water and urea permeability properties of *Xenopus* oocytes: expression of mRNA from toad urinary bladder. *Am J Physiol* **260**, C26–C34.

74 Yaneff A, Sigaut L, Gómez N, Aliaga Fandiño C, Alleva K, Pietrasanta LI & Amodeo G (2016) Loop B serine of a plasma membrane aquaporin type PIP2 but not PIP1 plays a key role in pH sensing. *Biochim Biophys Acta* **1858**, 2778–2787.